Phosphoproteome Profiling of the Receptor Tyrosine Kinase MuSK Identifies Tyrosine Phosphorylation of Rab GTPases

Authors

Hanna G. Budayeva, Arundhati Sengupta-Ghosh, Lilian Phu, John G. Moffat, Gai Ayalon, and Donald S. Kirkpatrick

Correspondence

budayeva.hanna@gene.com; dkirkpatrick@interlinetx.com

Graphical Abstract

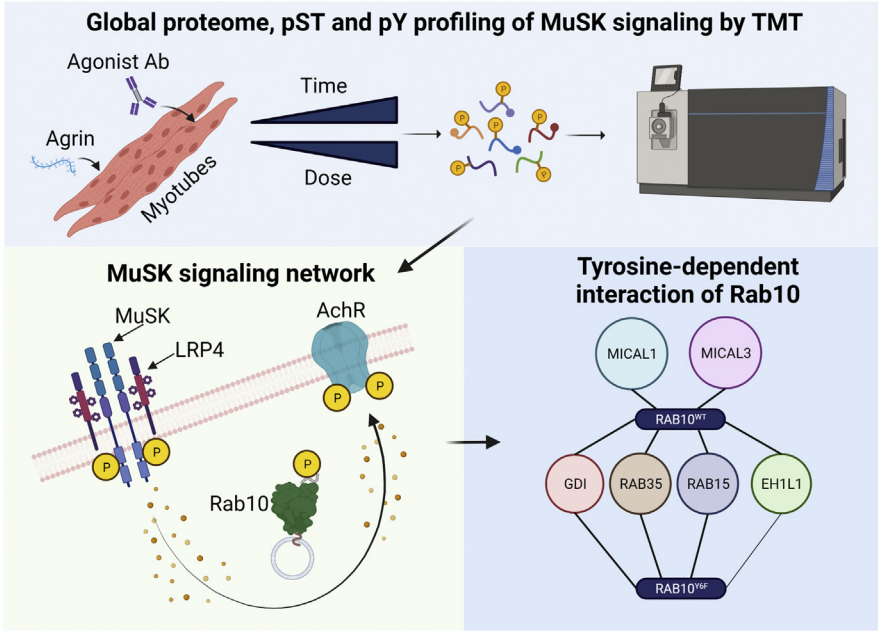

In Brief

We elucidated phosphosignaling network downstream of muscle-specific receptor tyrosine kinase (MuSK) activated by natural agonist agrin or agonist antibody. Dose–response and time-course experiments showed that both agonists elicited similar intracellular responses. We also characterized two small-molecule inhibitors of MuSK that effectively disrupted MuSK signaling pathway. We further studied the functions of MuSK-responsive tyrosine phosphorylation sites localized on several Rab GTPases. We showed that Rab10 Y6F mutation disrupts association with its adaptor molecules Micals.

Highlights

- Different agonists of muscle-specific kinase (MuSK) elicit similar phosphoprofiles.
- MuSK activation induces tyrosine phosphorylation of several Rab GTPases.
- MuSK inhibitors diminish receptor signaling, including phosphorylation on Rab10 Y6.
- Mutation of Rab10 Y6 disrupts its association with Mical adaptor proteins.

2022, Mol Cell Proteomics *21*(*4*), 100221
© 2022 THE AUTHORS. Published by Elsevier Inc on behalf of American Society for Biochemistry and Molecular Biology. This is an open access article under the CC BY-NC-ND license (http://creativecommons.org/licenses/by-nc-nd/4.0/).
https://doi.org/10.1016/j.mcpro.2022.100221

Phosphoproteome Profiling of the Receptor Tyrosine Kinase MuSK Identifies Tyrosine Phosphorylation of Rab GTPases

Hanna G. Budayeva[1,*], Arundhati Sengupta-Ghosh[2], Lilian Phu[1], John G. Moffat[3], Gai Ayalon[2], and Donald S. Kirkpatrick[1,*]

Muscle-specific receptor tyrosine kinase (MuSK) agonist antibodies were developed 2 decades ago to explore the benefits of receptor activation at the neuromuscular junction. Unlike agrin, the endogenous agonist of MuSK, agonist antibodies function independently of its coreceptor low-density lipoprotein receptor–related protein 4 to delay the onset of muscle denervation in mouse models of ALS. Here, we performed dose–response and time-course experiments on myotubes to systematically compare site-specific phosphorylation downstream of each agonist. Remarkably, both agonists elicited similar intracellular responses at known and newly identified MuSK signaling components. Among these was inducible tyrosine phosphorylation of multiple Rab GTPases that was blocked by MuSK inhibition. Importantly, mutation of this site in Rab10 disrupts association with its effector proteins, molecule interacting with CasL 1/3. Together, these data provide in-depth characterization of MuSK signaling, describe two novel MuSK inhibitors, and expose phosphorylation of Rab GTPases downstream of receptor tyrosine kinase activation in myotubes.

Muscle-specific receptor tyrosine kinase (MuSK) plays an essential role in the formation of neuromuscular junctions (1). Disruption of MuSK signaling is associated with neuromuscular diseases, such as myasthenia gravis and congenital myasthenia. Myasthenia gravis is a chronic autoimmune disease with an incidence rate of 0.3 to 2.8/100,000 that is commonly characterized by the presence of autoantibodies targeting different components of the MuSK signaling pathway (2, 3). Similarly, congenital myasthenic syndromes are a group of inherited disorders characterized by mutations in genes that function within the MuSK pathway (3).

Establishment of a neuromuscular junction *via* MuSK activation is a tightly orchestrated process with several layers of regulation. When a motor neuron reaches the muscle surface, it releases the proteoglycan signaling molecule agrin, which binds to MuSK coreceptor low-density lipoprotein receptor–related protein 4 (LRP4), leading to rearrangement and allosteric activation of the MuSK signaling complex (4, 5). These changes trigger autophosphorylation in the juxtamembrane regulatory site of MuSK and in its kinase domain (6), followed by recruitment of the adaptor molecule docking protein 7 (Dok7) (7). MuSK signaling propagates back to the plasma membrane, which results in phosphorylation and aggregation of acetylcholine receptor (AchR) ion channels on the muscle surface (8). Gating of AchR channel activity by neuron-secreted acetylcholine molecules regulates transmission of electric impulses from nerve to muscle (1). *MUSK* gene knockout in mice results in perinatal lethality because of aberrant neuromuscular synapse formation in the diaphragm (9).

Early on, it was recognized that agrin binds to a secondary molecule preceding MuSK activation (10). For almost a decade prior to the discovery of LRP4 (4, 5), MuSK-activating antibody (Ab) was employed to study the potential therapeutic value of receptor activation by direct Ab binding (11). In two recent studies, this Ab was demonstrated to act in an LRP4-independent manner in mouse models of ALS (12, 13). Both studies reported a delayed denervation upon treatment with the MuSK agonist Ab, with notable differences in downstream functional outcomes. Given these observations, we elected to utilize the agonist Ab as a tool to compare direct receptor activation *versus* coreceptor sequestration and assess to what degree does Ab-mediated MuSK activation recapitulates the physiological agrin-mediated activation in its broader scope of cellular responses beyond AchR clustering.

To this end, we employed orthogonal quantification of serine, threonine, and tyrosine phosphorylation signaling

From the [1]Microchemistry, Proteomics, and Lipidomics Department, [2]Neuroscience Department, and [3]Biochemical and Cellular Pharmacology and Computational Drug Design, Genentech, Inc, South San Francisco, California, USA
*For correspondence: Hanna G. Budayeva, budayeva.hanna@gene.com; Donald S. Kirkpatrick, dkirkpatrick@interlinetx.com.
Present address for [Donald S. Kirkpatrick]: Interline Therapeutics, South San Francisco, CA 94080, USA.
Present address for [Gai Ayalon]: Neumora Therapeutics, Brisbane, CA 94005, USA.

© 2022 THE AUTHORS. Published by Elsevier Inc on behalf of American Society for Biochemistry and Molecular Biology.
This is an open access article under the CC BY-NC-ND license (http://creativecommons.org/licenses/by-nc-nd/4.0/).

https://doi.org/10.1016/j.mcpro.2022.100221

downstream of agrin and MuSK agonist Ab in time-course and dose–response experiments. The results elucidated remarkably similar downstream phosphorylation cascades, represented primarily by tyrosine phosphorylation. Our findings confirm previously reported activation of MuSK, Dok7, and AchR on a series of phosphorylation sites. We also observed novel MuSK phosphorylation in the ATP-binding region of the kinase and described the activity of two potent MuSK small-molecule kinase inhibitors. Importantly, this revealed a novel Rab10 tyrosine phosphorylation at Y6 induced by both agonist Ab and endogenous ligand. We show that the conserved tyrosine in the N-terminal region of Rabs modulates binding of Rab effector molecules, molecule interacting with CasL 1 (Mical1) and Mical3.

EXPERIMENTAL PROCEDURES

Cell Lines

C2C12 myoblasts were obtained from the American Type Culture Collection and maintained in Dulbecco's modified Eagle's medium supplemented with 10% fetal bovine serum and GlutaMAX. For differentiation, C2C12 normal growth media were replaced with low serum media (2% horse serum). Myoblasts were differentiated until the appearance of myotubes (4–7 days) with differentiation media changed every other day.

Reagents

Recombinant rat agrin protein was obtained from R&D Systems. MuSK activating Ab (Ab#13) is human variable/mouse constant chimeric Ab generated from human naïve phage library as previously described (11, 13). Small-molecule kinase inhibitor AZ-23 was purchased from MedChem Express; compound 28 was synthesized in-house according to published method (14). The following primary antibodies were used for Western blotting (WB): rabbit anti-phosphotyrosine (Cell Signaling), rabbit antihemagglutinin (HA) (Cell Signaling), and rabbit anti-Mical1 (Abcam). Light chain–specific secondary anti–rabbit-horseradish peroxidase Ab was obtained from Jackson Laboratory.

Generation of C2C12 Cell Lines Expressing HA-Rab10

Mouse Rab10 wt or Rab10 Y6F ORF with N-terminal green enhanced Nano-Lantern-HA sequences were synthesized and cloned into PiggyBac-compatible expression vectors containing TRE3GS-TetON promoter and puromycin resistance cassette (BH1.4). C2C12 cells were transfected with PiggyBac transposase expression plasmid (pBO; Transposagen) and corresponding BH1.4 at 1:3 pBO:BH1.4 ratio using FuGene HD (Promega) transfection reagent according to manufacturer's protocol. C2C12 cells were selected with 2 μg/ml puromycin (Sigma–Aldrich) for 4 days after transfection. To induce Rab10 expression, cells were treated with 0.5 μg/ml doxycycline (Sigma–Aldrich) for 2 days.

AchR Clustering Assay

Differentiated C2C12 myotubes were treated as indicated for 8 to 16 h in differentiation media. For visualization of AchR clusters, cells were incubated with Bungarotoxin–Alexa Fluor 488 conjugate for 30 min at 37 °C in differentiation media. After incubation, cells were washed with PBS and fixed with 4% formaldehyde in PBS for 15 min at room temperature. Imaging was performed on InCell 6000 high-content imaging system, and manufacturer's software was used for quantification of AchR clusters and nuclei in each myotube. Cluster size was filtered to ≥5 nm. The ratio of the total counted AchR clusters per myotube to the total number of nuclei per myotube was used for normalization between conditions.

Experimental Design and Statistical Rationale—Dose–response and time-course experiments were performed in two and four biological replicates, respectively. Each biological replicate experiment included one control (untreated sample). MSstats tandem mass tag (TMT) R package was used for summarization and modeling of the global and phosphosite-level TMT data. The following parameters were used for analysis: Tukey's median polish as peptide to protein summarization method, global median normalization (equalize median parameter), moderated *t* test for hypothesis testing, and Benjamini–Hochberg adjustment method for multiple comparisons.

Global Proteome and Phosphoproteome Profiling

In two replicates of the dose–response experiment, C2C12 myotubes differentiated for 6 days were treated with agrin (0.01, 0.1, 1, 5, or 10 nM), MuSK Ab#13 (0.5, 5, 50, 100, and 400 nM), or untreated (not treated [NT]) in differentiation media for 30 min. In four replicates of the time-course experiments, myotubes were treated with 10 nM agrin or 400 nM agonist Ab for 10, 30, 60, and 120 min or incubated in differentiation media without treatment (NT). Treatment with small-molecule kinase inhibitors was performed at indicated concentrations for 1 h before agonist treatment at 10 nM agrin or 400 nM Ab#13 in one biological replicate and analyzed by mass spectrometry (MS) in duplicate. Cells were collected by scraping into lysis buffer (9 M urea, 50 mM Hepes [pH 8.0], 150 mM NaCl, and phosphatase inhibitor cocktail [Roche]). After microtip sonication, the lysates were cleared by centrifugation. Protein concentration was determined by bicinchoninic acid assay in the soluble fraction, and equal total amounts of protein (30 mg per sample) were subjected to further processing. Protein mixtures were reduced in 10 mM DTT (Thermo Fisher Scientific) and alkylated in 30 mM iodoacetamide (Sigma–Aldrich). Samples were diluted fourfold with 50 mM Hepes prior to digestion with LysC (Fujifilm Wako Chemical Corporation) at 1:100 enzyme:protein ratio overnight at 37 °C, followed by Pierce trypsin (Thermo Fisher Scientific) digestion at 1:100 ratio for 8 h at 37 °C. After digestion, samples were acidified with 1% Pierce TFA (Thermo Fisher Scientific), and any precipitated undigested material was removed by centrifugation. Peptides were desalted using C18 SepPak column according to manufacturer's protocol. An aliquot of each desalted peptide mixture (100 μg each) was used for TMT-based quantification of total protein levels. The remaining peptides were lyophilized and subjected to phosphopeptide enrichment using 100 mg titansphere Phos-TiO_2 columns (GL Sciences) according to manufacturer's protocol. Isolated peptides were desalted by C18 SepPak column and labeled with TMT 10plex or TMT 11plex reagents (Thermo Fisher Scientific) using manufacturer's protocol. Samples were pooled after confirming that TMT incorporation rate reached >98% as assessed by a small-scale MS analysis. Combined samples were subjected to phosphotyrosine enrichment using P-Tyr-1000 PTMScan kit (Cell Signaling Technology). Eluted peptides (containing phosphotyrosine-enriched peptides) were desalted prior to LC–MS analysis. PTMScan flow-through fraction (containing remaining phosphorylated peptides) was desalted, subjected to fractionation by basic pH reversed-phase liquid chromatography on Agilent into 12 total fractions as described previously (15) and desalted by C18 PhyTip columns (PhyNexus) using PhyNexus MEA robot prior to LC–MS analysis.

MS Analysis of TMT Samples

Dried TMT-labeled samples from global proteome and phosphoproteome profiling experiments were reconstituted in 2% acetonitrile/0.1% formic acid (buffer A) for LC–MS analysis on Dionex Ultimate

3000 RSLCnano system (Thermo Fisher Scientific, Inc) and Orbitrap Fusion Lumos Tribrid MS (Thermo Fisher Scientific, Inc). Peptides were resolved on 100 μm ID PicoFrit column packed with 1.7 μm Acquity BEH (New Objective) by 160 min linear gradient of 2% to 30% buffer B (98% acetonitrile/0.1% formic acid) in buffer A (2% acetonitrile/0.1% formic acid) at a flow rate of 450 nl/min. Multinotch MS3-based TMT method was used for analysis. Each duty cycle included an MS1 scan in the Orbitrap at 120,000 resolution across 350 to 1350 *m/z* range with automatic gain control (AGC) target of 1.0e6 and maximum injection time of 50 ms. Data-dependent ion trap MS2 scans were performed on the top 10 peptides with collision-induced dissociation activation, 0.5 *m/z* isolation window in quadrupole, turbo scan rate, AGC target of 2.0e4, maximum injection time of 100 ms. Eight MS2 fragment ions were selected for Orbitrap synchronous precursor selection MS/MS/MS (SPS-MS3) scans with isolation widths of 2 *m/z* using isolation waveforms with multiple frequency notches as previously described (16). These ions were fragmented during MS3 by high-energy collision–induced dissociation and analyzed by Orbitrap at 50,000 resolution, AGC target of 2.5e5, and maximum injection time of 150 ms.

MS TMT Data Analysis

MS2 spectra were searched using Mascot (Matrix Sciences) against a target-decoy database that included UniProt *Mus musculus* protein sequences (June 2016 version, 89,340 entries), known contaminants, and the reversed protein sequences. Search parameters included precursor ion mass tolerance of 50 ppm, fragment ion tolerance of 0.8 Da, and tryptic specificity with up to two missed cleavages permitted. The following fixed modifications were considered: carbamidomethylation on cysteines (+57.0215 Da) and TMT modification on the N terminus and lysines (+229.1629 Da). Variable modifications included methionine oxidation (+15.9949 Da), phosphorylation on serine/threonine/tyrosine (+79.9663 Da), and TMT modification on tyrosine (+229.1629 Da). Peptide level and protein level search results were filtered to <1% false discovery rate (FDR) and <2% FDR, respectively, using previously described algorithms (17). Ascore algorithm (18) was used for assigning phosphorylation site localization probabilities. Prior to modeling, phosphopeptides spanning the same phosphorylation site(s) but containing various other analytical modifications were collapsed under a single phosphopeptide feature. In those cases when a phosphorylation site was identified alone, as well as in combination with another phosphosite, the two phosphopeptide features containing single and double phosphorylation events, respectively, were analyzed separately. MSstatsTMT R package was used for summarization and modeling of the global and phosphosite-level TMT data.

To compare the number of identified phosphorylated proteins between the dataset collected in this study and Dürnberger *et al.* dataset (19), protein names were extracted from the supplemental table supp_M113.036087_mcp.M113.036087-1, "quantifiedPhosphoPeptides" tab. Next, protein names of the phosphorylated proteins profiled in the two studies were matched and indicated as "phosphoprotein groups" in supplemental Fig. S1.

Immunoaffinity Purification

For isolation of Rab10 and interacting proteins, C2C12 cells expressing HA-Rab10 wt or HA-Rab10 Y6F mutant were lysed at 4 °C in 1% NP-40 buffer (50 mM Tris–HCl, pH 7.5, 120 mM NaCl, 1 mM EDTA, 1% NP-40, protease and phosphatase inhibitor cocktail [Roche]). Lysates were processed using rotor stator homogenizer (OMNI International), and insoluble fraction was removed by centrifugation at 11,000*g* for 10 min. Protein concentration was measured by Pierce bicinchoninic acid protein assay kit (Thermo Fisher Scientific), and 1 mg of total protein per condition was used for immunoaffinity purification (IP) with Pierce anti-HA agarose (Thermo Fisher Scientific). After 2 h of incubation, beads were washed three times with lysis buffer, followed by PBS wash. Isolated protein complexes were eluted with 2× Bolt lithium dodecyl sulfate sample buffer (Thermo Fisher Scientific) by shaking at 70 °C for 10 min. Eluted protein mixtures were reduced and alkylated with 50 mM DTT and 30 mM iodoacetamide, respectively. For WB analysis of IP samples, approximately 20% of the eluted protein mixtures or 15 μg of soluble fraction from total cell lysates were resolved by 4 to 12% NuPAGE Bis–Tris gel (Invitrogen). Proteins were transferred to a nitrocellulose membrane using iBlot system (Invitrogen). Membranes were incubated with animal-free blocking solution (Cell Signaling Technologies) for 1 h at room temperature, followed by incubation with indicated primary and secondary antibodies. Horseradish peroxidase signal was detected by ECL or ECL Prime reagent (GE Healthcare Life Sciences) used as directed and acquired by iBright imaging system (Invitrogen). Relative quantification of protein bands from WBs was performed with ImageJ (NIH) (20).

MS Analysis of IP Samples

For IP–MS analysis of isolated complexes, samples in 1× lithium dodecyl sulfate sample buffer were briefly resolved by Bolt 4 to 12% Bis–Tris gel, and two bands per lane were excised and processed for trypsin in-gel digestion as previously described (21). Lyophilized peptides were reconstituted in buffer A and resolved by reverse-phase chromatography on a Dionex Ultimate 3000 RSLCnano system (Thermo Fisher Scientific, Inc) over 40 min gradient and 0.3 μl/min flow rate as described previously. MS analysis was performed by Orbitrap Fusion Lumos Tribrid MS (Thermo Fisher Scientific, Inc). Precursor ions were analyzed by Fourier transform MS at 240,000 resolution, with a maximum injection time of 50 ms, and AGC target of 1e6. Precursor ions were fragmented by collision-induced dissociation, and MS/MS data were acquired in ion trap in data-dependent mode with a maximum injection time of 11 ms and an AGC target of 2e5.

MS2 spectra were searched using Mascot algorithm (Matrix Sciences) against a target-decoy database that included UniProt *M. musculus* protein sequences (June 2016 version), Rab10 Y6F mutant sequence, known contaminants, and the reversed protein sequences. Search parameters included 50 ppm precursor ion mass tolerance, 0.8 Da fragment ion tolerance, and tryptic specificity with up to two missed cleavages permitted. Fixed modification included carbamidomethylation on cysteines (+57.0215 Da). Variable modification included methionine oxidation (+15.9949 Da). Peptide level and protein level search results were filtered to <1% FDR and <2% FDR, respectively, using previously described algorithms (17).

Interaction specificity and relative abundance analyses from three replicate experiments were performed with VistaQuant (22) for peptide MS1 area under the curve crossquantification, followed by statistical analysis with MSstats R package (23).

In vitro *Kinase Activity Assay*

Kinase activity profiling was performed at Thermo Fisher Scientific as part of SelectScreen service; for the full list of kinases profiled, see supplemental Table S2. Percent inhibition was calculated based on FRET emission ratio, as described by the manufacturer.

Sequence Alignment

Indicated protein sequences were derived from UniProt (release 2020_02) and aligned using Clustal Omega program (Conway Institute) (24). Figures were generated using BOXSHADE.

RESULTS

Time-resolved and Dose-dependent Phosphoprofiling of MuSK Signaling in Myotubes

C2C12 myoblasts differentiated into myotubes were used as a model system to characterize signal propagation downstream of MuSK activation by agrin and MuSK-activating Ab (Ab#13). Activation of MuSK in cell culture was validated by imaging AchR clustering after treatment with each agonist (Fig. 1*A*). Automated high-content imaging was used to quantify the number of AchR clusters formed in response to a dose curve of each agonist. These data demonstrated maximal AchR clustering beginning at doses of 0.1 nM agrin and 5 nM Ab#13 at the 16 h time point (Fig. 1*B*). Based on this, a range of agonist concentrations and a set of time points were selected to reflect minimal and maximal as well as early and late pathway responses to agonist treatments. Next, two orthogonal approaches were applied to profile MuSK-specific signaling whereby phosphorylation events were quantified

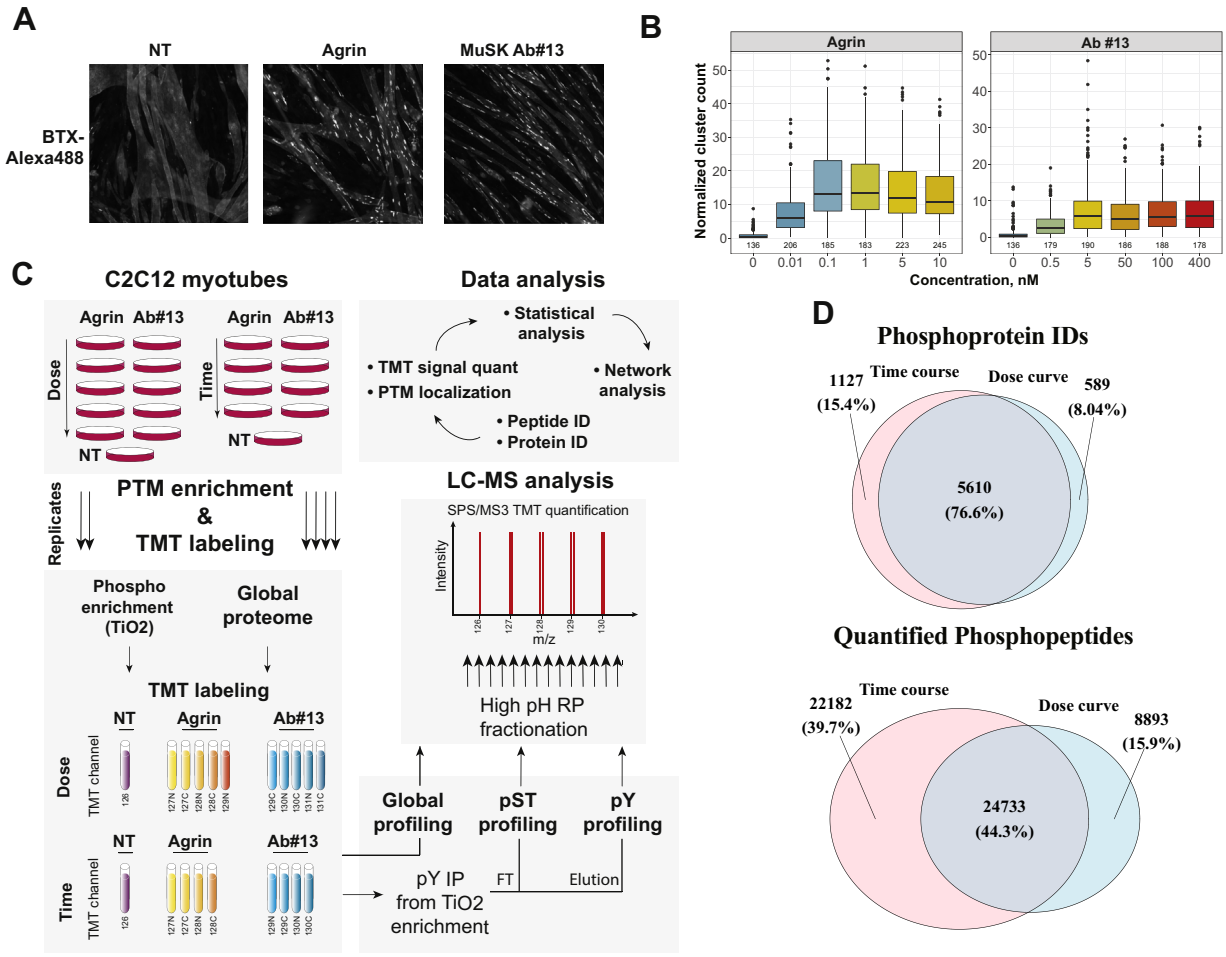

FIG. 1. **An orthogonal approach for characterization of MuSK signaling utilizes time-resolved and dose-dependent phosphoproteome profiling in myotubes.** *A*, C2C12 myotubes were treated with recombinant agrin (10 nM), MuSK Ab#13 (400 nM), or untreated (NT) for 16 h and acetylcholine receptor clusters stained with Bungarotoxin–Alexa Fluor 488 conjugate. Images were collected on In Cell Analyzer 6000. Representative images from three biological replicates are shown. *B*, C2C12 myotubes were treated with agrin or MuSK Ab#13 at indicated concentrations for 16 h and processed as in (*A*). Data are represented as cluster counts per myotube normalized to the number of nuclei per myotube. Median values are indicated within each box plot. Number of quantified myotubes per condition is indicated under the box plots (n = 3). *C*, a workflow for TMT-based relative quantification of time-resolved and dose-dependent changes in phosphorylation levels on S/T/Y and total protein levels. In the dose–response experiment, C2C12 myotubes were treated with agrin (0.01, 0.1, 1, 5, or 10 nM), MuSK agonist antibody (0.5, 5, 50, 100, and 400 nM), or untreated (NT) in differentiation media for 30 min (n = 2). In the time-course experiment, C2C12 myotubes were treated with recombinant agrin (10 nM) or MuSK Ab#13 (400 nM) for 10, 30, 60, and 120 min or untreated (NT) in differentiation media (n = 4). *D*, Venn diagrams showing the total number of phosphorylated proteins and the total number of phosphopeptide features quantified in four replicates of time course and two replicates of dose curve phosphorylation profiling experiments. For quantitative analysis, phosphopeptides containing the same phosphorylation site(s) but containing various other analytical modifications were collapsed under a single phosphopeptide feature. Phosphopeptides with at least one phosphosite with Ascore ≥10 (>90% probability of localizations) were included in the diagram. Fraction of the total identifications (IDs) are indicated in the parentheses. Ab, antibody; MuSK, muscle-specific receptor tyrosine kinase; NT, not treated; TMT, tandem mass tag.

across a time course and dose response following activation with either agrin or Ab#13 (Fig. 1*C*). In the dose–response experiment, myotubes were activated for 30 min with each dose of the agonist or were incubated in media without treatment (NT) prior to denaturing cell lysis. In the time-course experiment, lysates were collected at 10, 30, 60, and 120 min time points following treatment with the highest concentrations of each agonist used in the dose–response experiment. Phosphopeptides were isolated using TiO_2 chromatography, and the phosphotyrosine fraction further enriched using the PTMScan pY1000 kit. TMT-based quantification *via* SPS-MS3 was used to determine relative phosphopeptide abundances between conditions. TMT analysis by SPS-MS3 was previously shown to improve data quality by accumulating signal from multiple fragment ions for MS3 events while reducing noise stemming from coisolation of interfering ion species in MS2-based quantitation (16, 25). In parallel, protein abundances were monitored across conditions using global proteome profiling to highlight changes occurring because of alterations in protein levels rather than altered phosphosite occupancy. An interactive dashboard is available for visualization and exploration of the datasets (https://sld-acs-sf.sf.perkinelmercloud.com/spotfire/wp/analysis?file=/Guest/MuSK_GlobalPhosphoProfiling&waid=7O5olDRpMUK6wRIS-ieLw-201250ef41XBf8&wavid=0; TIBCO Spotfire dashboard). Across all the experiments combined, 7326 phosphoproteins were quantified, and localization probabilities were assigned to phosphorylation sites by the Ascore algorithm (18), resulting in 67,945 phosphopeptide features (supplemental Table S1). Within the quantified phosphopeptides, ~80% phosphorylation sites had localization probability >90% (Ascore ≥10; 55,808 p-sites) (Fig. 1*D*). This analysis extends substantially on previous global study of MuSK signaling in C2C12 myotubes (19) by profiling phosphorylation status of 4933 additional protein groups (supplemental Fig. S1).

Natural Agonist Agrin and MuSK Agonist Ab Induce Tyrosine Phosphorylation in ATP-binding Region of the Receptor

Results of the MuSK phosphoprofiling study reveal that both agonists induce remarkably similar changes in MuSK activation (Fig. 2*A*). Phosphosite-level correlation of $r = 0.55$ was observed between agrin and Ab#13 treatments at the highest concentrations of each molecule. Phosphorylation changes were consistently independent of protein level changes, as indicated by the absence of correlation between the log2 ratios of phosphosite levels and total protein levels upon treatment with each agonist ($r = 0.01$ for agrin and $r = 0.02$ for agonist Ab treatments) (supplemental Fig. S2).

Several known components of the MuSK signaling pathway were observed in the dose–response and time-course phosphoprofiling datasets, indicative of MuSK activation. MuSK adaptor protein Dok7 (DOK7) was phosphorylated at Y396 and Y405 in agonist concentration–dependent manner (Fig. 2*B*). In addition, inducible phosphorylation of AchRβ (ACHB) and AchRδ (ACHD) subunits, known to regulate aggregation of the AchR clusters (8, 26), was detected on Y390 and Y393, respectively (Fig. 2*C*). A number of MuSK phosphorylation sites were also quantified, some of which responded to agonist treatment (Fig. 2, *D–F*). Dose-dependent increases in MuSK phosphorylation were observed at the Y553 regulatory site juxtaposed to the plasma membrane as well as at phosphosites localized in the kinase activation loop of the receptor (Y750, S751, Y754, and Y755) (Fig. 2*E*). In addition, a novel tyrosine phosphorylation event on Y599 was detected at the ATP-binding region of MuSK (Fig. 2*D*) and shown to increase in a dose-dependent manner (Fig. 2*E*). This region was previously observed to contain the Y576 phosphorylation site (6), which was identified in this study as well (Fig. 2*F*). Interestingly, unlike other MuSK tyrosine phosphorylation sites, Y576 and Y599 displayed delayed phosphorylation kinetics in the time-course experiment relative to other MuSK phosphorylation sites (Fig. 2*F*). These residues are highly conserved in different species but are not present in the sequences of receptor tyrosine kinases that are most closely evolutionarily related to MuSK (27) (Fig. 2*G*). Therefore, our approach allowed identification of MuSK-dependent tyrosine phosphorylation events in the ATP-binding region of the receptor, whose unique functions are yet to be defined.

MuSK Activation–dependent Phosphorylation Pathway

To reconstruct the MuSK-specific signaling cascade, we focused on 112 phosphorylation events that were increased more than twofold in at least one condition in both dose–response and time-course experiments. Pearson correlation–based analysis was applied to rank phosphorylation events displaying dose-dependent increases upon treatment with each MuSK agonist in relation to Dok7 Y396 phosphorylation (Fig. 3*A*). The preliminary list of MuSK-dependent phosphorylation events included 53 phosphopeptide features based on a line similarity score cutoff of 0.4 (Fig. 3*B* and supplemental Table S1). Approximately, 75% of these sites were on tyrosine residues, whereas the rest were a mix of serine and threonine.

A majority of the phosphorylation profiles in the MuSK signaling network were sustained responders or phosphosites that increased by more than twofold as early as 10 min after agonist treatment and remained elevated throughout the time course in comparison to unstimulated cells (Fig. 3*B*). Such events include the MuSK Y553 site, MuSK activation loop sites (Y750 and Y754), and Dok7 adaptor protein sites (Y396 and Y406) (Fig. 3*B*). Phosphorylation of Sorbs2 (sorbin and SH3 domain–containing protein 2) on Y1176 in response to MuSK activation is a newly identified event, although Sorbs proteins have previously been shown to function immediately downstream of MuSK (28). Sustained phosphorylation was observed on multiple AchR subunits, as well as syntrophin proteins SNTA1 and SNTB1, and pleckstrin homology–like

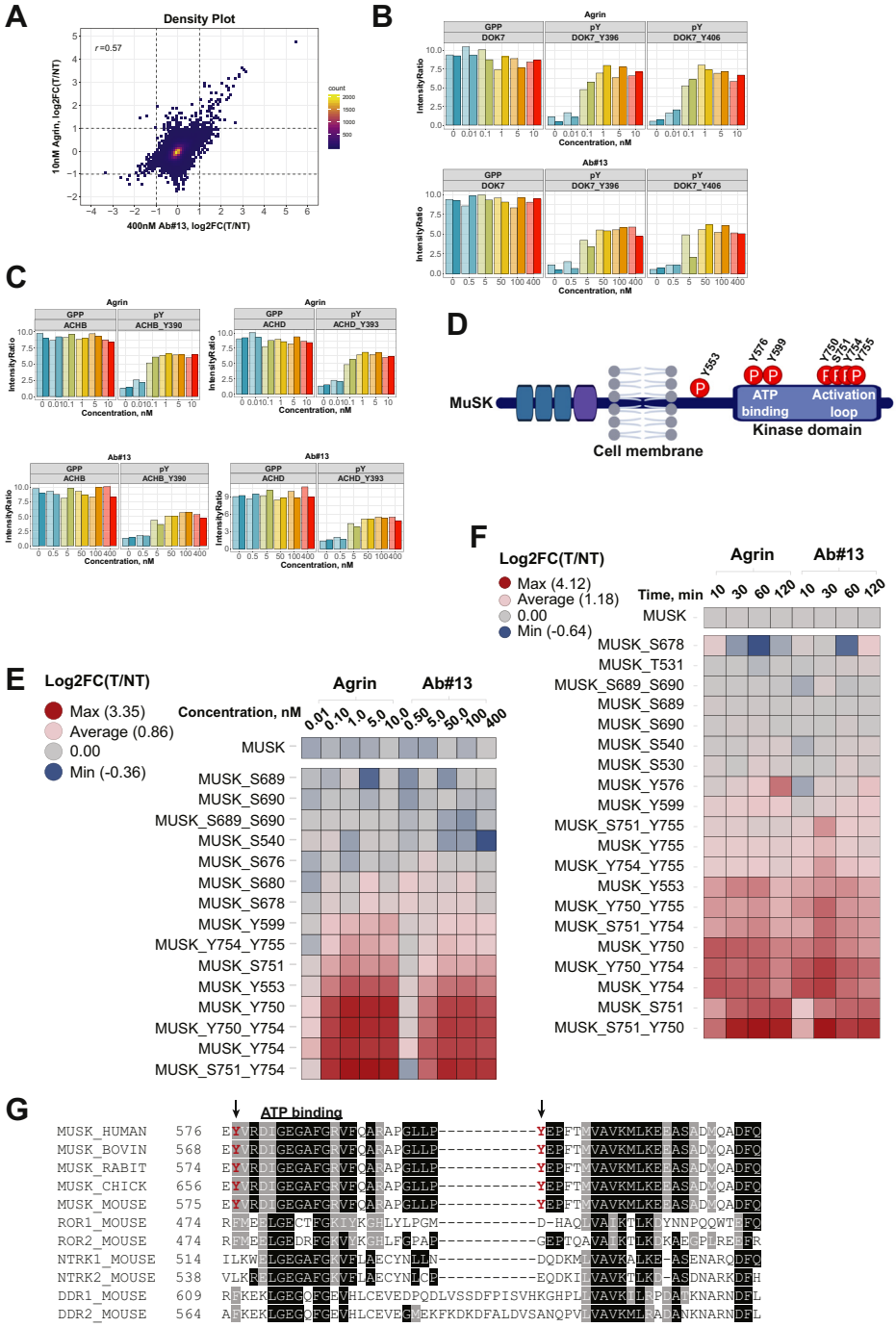

FIG. 2. **Agrin and MuSK-activating antibodies induce similar phosphorylation cascades that include newly identified MuSK Y599 phosphorylation event.** *A*, density plot comparing changes in site-specific phosphorylation induced by two MuSK agonists. *r* is Pearson correlation coefficient of log2FC between indicated conditions, n = 31,903 observations across duplicate experiments. *B* and *C*, relative TMT channel intensities for indicated global proteome profiling (GPP) and tyrosine phosphorylation (pY) quantified in duplicate experiments across indicated doses of agrin and Ab#13. *D*, coverage of MuSK phosphorylation sites that responded to agonist treatment. *E* and *F*, heatmaps of log2FC (agonist *versus* NT) in MuSK phosphorylation by site and total MuSK protein quantified in phosphoproteome and GPP analyses of agonist dose response in duplicate and time course in four replicates, respectively. *G*, sequence alignment of MuSK ATP-binding domain across species and closely related tyrosine kinases generated with the Clustal Omega program and BOXSHADE. Ab, antibody; FC, fold change; MuSK, muscle-specific receptor tyrosine kinase; NT, not treated; TMT, tandem mass tag.

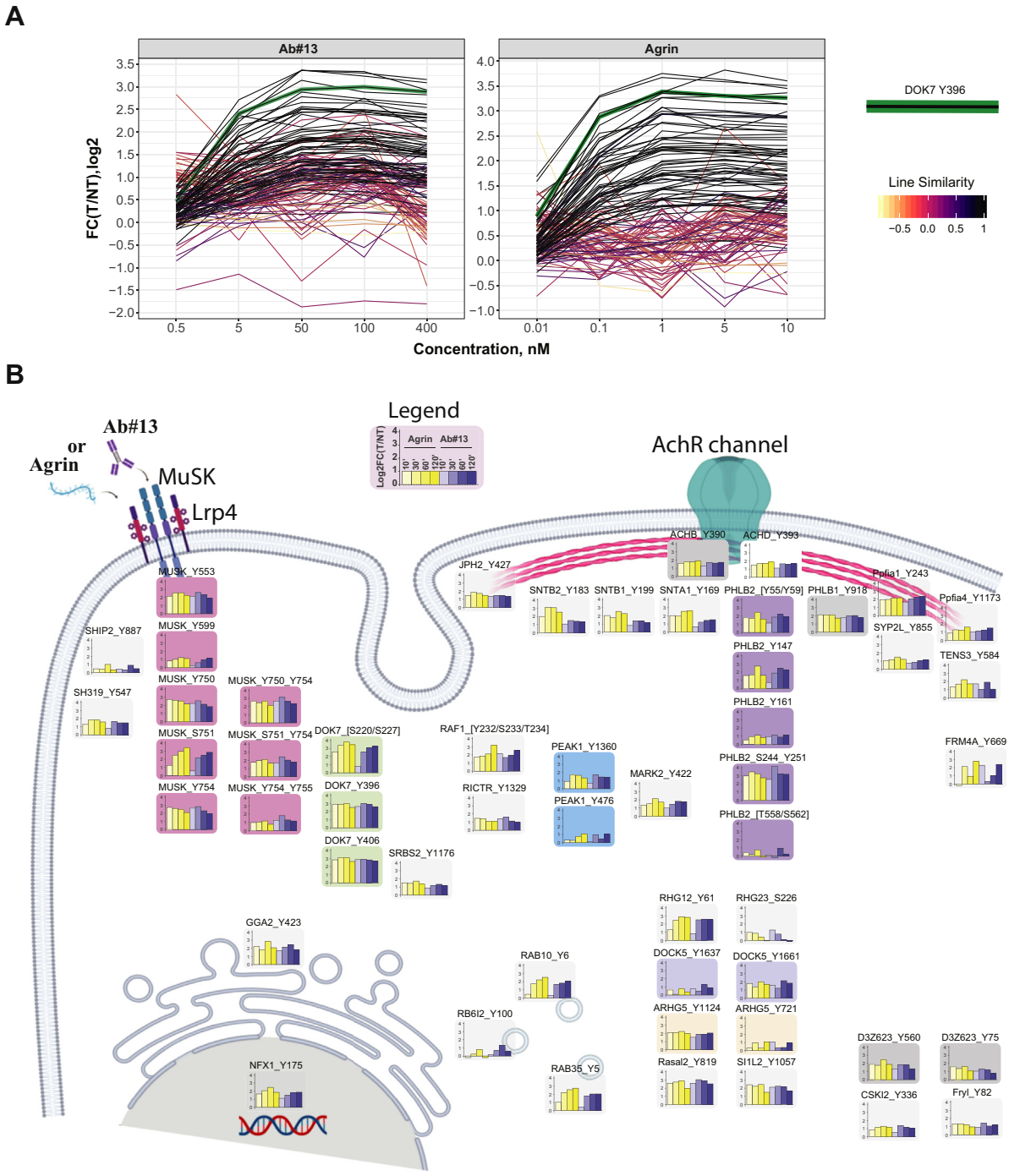

FIG. 3. **Time-resolved phosphorylation cascade of MuSK activation.** *A*, dose–response profiles of 119 phosphopeptide features reporting twofold or greater increase in at least one condition from both experiments performed in duplicate. Pearson correlation–based analysis was used to assign linear similarity coefficients relative to the DOK7 Y396 phosphorylation profile highlighted in *green*. *B*, schematic representation of time-resolved phosphorylation events downstream of MuSK activation by agrin and Ab#13. Plots for each node report log2 fold changes at indicated phosphosites relative to untreated cells across a time course of treatment with each agonist in four replicate experiments. Statistical modeling was performed with MSstatsTMT R package. Ab, Antibody; DOK7, docking protein 7; MuSK, muscle-specific receptor tyrosine kinase.

family members PHLB2 and PHLB1. These actin-associated cytoskeletal proteins play a role in AchR clustering (29, 30), but their modification by tyrosine phosphorylation has not been previously reported in relation to MuSK signaling. In addition, we identified novel phosphorylation sites that could play a role in regulating cytoskeletal and focal adhesion–mediated reorganization of postsynaptic apparatus of the muscle membrane. These include synaptopodin-like protein

(SYP2L), tensin (TENS3), and liprin-α isoforms phosphorylated at homologous tyrosine residues (Ppfia1 Y243 and Ppfia4 Y1173). A potentially important node for regulation of calcium signaling in activated muscle was represented by Y427 phosphorylation on junctophilin 2, which is part of the junctional membrane complex linking the plasma membrane to the sarcoplasmic reticulum and coordinating intracellular calcium release channels in skeletal muscle (31).

Several identified proteins that respond to MuSK activation are known to function in Ras/MAPK signaling pathway. For instance, we detected MuSK-inducible phosphorylation on serine/threonine-protein kinase c-Raf (RAF1), a major mediator of Ras/MAPK signaling cascade. The largest category of phosphorylation events included regulators of guanine nucleotide exchange factors (DOCK5 and ARHG5) and GTPase activators (Rasal2/NGAP, RHG12, and RHG23). These proteins participate in processes regulated by the Ras superfamily of small GTPases, such as Rac, Rho, and Ras. In addition, mammalian target of rapamycin complex 2 regulatory subunit RICTOR was phosphorylated on Y1329 throughout the MuSK activation time course, a phosphosite with previously uncharacterized function.

We also observed signal propagation among proteins that function in vesicular trafficking between various intracellular membranes. SH2 domain–containing inositol phosphatase 2, which is recruited to the plasma membrane upon epidermal growth factor receptor activation and participates in receptor endocytosis (32), was phosphorylated on Y887 in response to treatment with each MuSK agonist. In addition, we observed MuSK activation–dependent phosphorylation of γ-adaptin ear-containing, ADP ribosylation factor–binding protein 2 (GGA2), a Golgi-localized sorting protein, and RB6I2, Rab6 effector protein with functions in trafficking from the Golgi apparatus to the plasma membrane (33). Interestingly, tyrosine phosphorylation near the N termini of small Ras-like GTPases Rab10 and Rab35 (Y6 and Y5, respectively) was increased at the later time points of the MuSK signaling response compared with the majority of the other signaling nodes quantified in this study. This observation prompted further investigation into the physiological consequences of Rab phosphorylation.

Tyrosine Phosphorylation of Endocytic Rab Proteins is Induced Upon MuSK Activation

We identified several sites of MuSK-inducible phosphorylation on Rab protein family members, including Rab8a, Rab10, Rab13, and Rab35 (Fig. 4*A*). All the sites responded to MuSK signaling at the later time points (30, 60, and 120 min) but not at the earliest time point (10 min) following agonist treatment. This tyrosine phosphorylation site in the N-terminal region of Rabs is conserved in approximately 40% of Rab family members (supplemental Fig. S3). Interestingly, all the

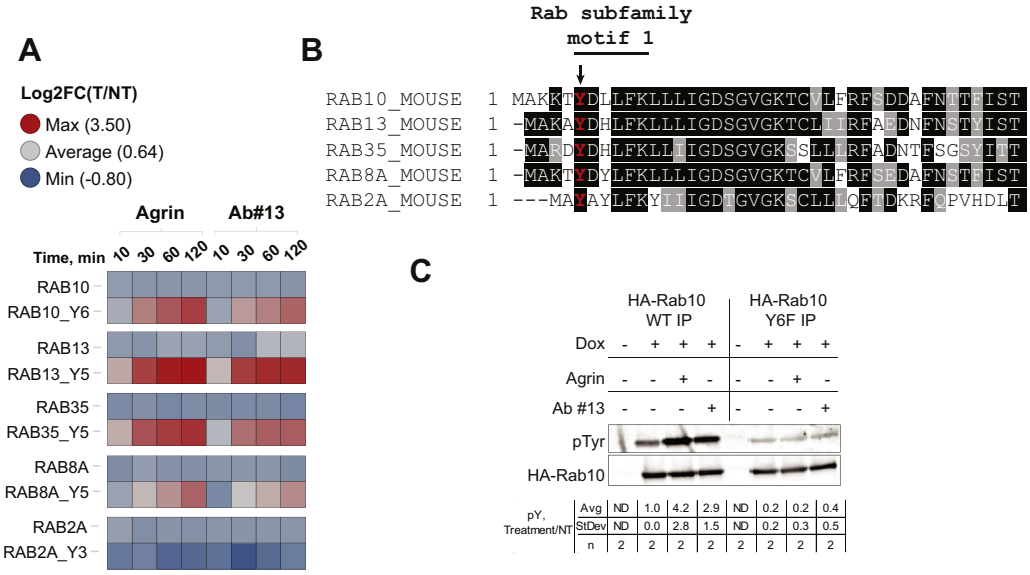

FIG. 4. **Tyrosine phosphorylation of endocytic Rabs.** *A*, a heatmap of log2 fold changes in tyrosine phosphorylation of Rab proteins in C2C12 myotubes during a time course of MuSK activation by 10 nM agrin or 400 nM Ab#13 *versus* untreated control. Statistical analysis was performed with MSstatsTMT R package based on data from four replicate experiments. *B*, alignment of N-terminal sequences of Rab proteins identified in this study. Alignment was generated with the Clustal Omega program and BOXSHADE. *C*, C2C12 myotubes expressing Dox-inducible HA-Rab10^{wt} or HA-Rab10^{Y6F} were treated with 10 nM agrin or 400 nM Ab#13 for 1 h, followed by HA IP. HA-Rab10 tyrosine phosphorylation levels were probed with antiphosphotyrosine antibody, whereas anti-HA antibody was used as a loading control for HA-Rab10. Antibody specificity was confirmed in control samples without Dox stimulation. Statistics table indicates treated/NT (NT = +Dox, no treatment) pY ratios normalized to total HA-Rab10 levels, measured by ImageJ. Ab, antibody; HA, hemagglutinin; IP, immunoaffinity purification; MuSK, muscle-specific receptor tyrosine kinase; TMT, tandem mass tag.

Rab tyrosine phosphorylation sites that responded to MuSK activation contained aspartate in +1 position (Fig. 4*B*). Moreover, a homologous tyrosine site on Rab2a Y3 that was detected and shown to be nonresponsive to MuSK activation (Fig. 4*A*) contained alanine in place of this aspartate (Fig. 4*B*). This observation reveals a common Rab tyrosine phosphorylation motif that potentially functions downstream of MuSK.

For further validation of Rab protein phosphorylation downstream of MuSK, C2C12 myoblasts were generated to express Dox-inducible HA-Rab10^{wt} or HA-Rab10^{Y6F} mutant tagged with HA at the N terminus. Mutation of tyrosine to phenylalanine preserves the aromatic ring in the side chain but eliminates the possibility of phosphorylation at this site. By IP–WB, we confirmed that HA-Rab10 is phosphorylated in the presence of agrin or Ab#13 and that this phosphorylation event is absent in HA-Rab10 Y6F mutant IP (Fig. 4*C*).

Rab10 Y6 Phosphorylation is Ablated by MuSK Inhibitors

To validate MuSK-inducible phosphorylation of Rabs, two ATP-competitive small-molecule inhibitors were identified that had been previously reported to inhibit MuSK activity *in vitro* (34). AZ-23 was originally characterized as a tropomyosin-related kinase (Trk) inhibitor, whereas compound 28 was discovered in a screen of interleukin-2-inducible T-cell kinase inhibitors (14). Both compounds inhibit ~99% of MuSK activity at 0.1 μM *in vitro* (Tables 1 and 2 and supplemental Table S2).

For further characterization of AZ-23 and compound 28 effects on MuSK pathway, we tested their ability to inhibit AchR clustering in C2C12 myotubes. Treatment with each kinase inhibitor impaired AchR clustering in a dose-dependent manner following agrin or Ab#13 stimulation (Fig. 5, *A* and *B*). Since AZ-23 demonstrated higher potency in blocking MuSK-dependent AchR clustering (Fig. 5*A*), we further tested its effect on the C2C12 phosphoproteome following MuSK stimulation. Myotubes were pretreated with two concentrations of AZ-23, followed by MuSK activation with each agonist for 30 min. Phosphotyrosine profiling resulted in quantification of 39 tyrosine kinases (Fig. 5, *C* and *D* and supplemental Table S1). Of these, only MuSK autophosphorylation sites displayed agonist inducible phosphorylation (Fig. 5, *C* and *D*, *left panel*). Furthermore, these increases were reversed by AZ-23 in a dose-dependent manner (Fig. 5, *C* and *D*). A similar profile was detected for Dok7, AchR subunits, and other signaling nodes identified in this study (supplemental Fig. S4). These findings support the claim that AZ-23 is a potent small-molecule inhibitor of MuSK activity in cells.

Unfortunately, Rab10 tyrosine phosphorylation was not detected in AZ-23 phosphoproteome profiling study because of the stochastic nature of data-dependent acquisition. To make up for this, we tested the effects of both small-molecule inhibitors by IP–WB to detect tyrosine phosphorylation on HA-Rab10. As predicted, AZ-23 and compound 28 successfully abolished Rab10 tyrosine phosphorylation in Ab#13-treated cells, further supporting the hypothesis that Rab N-terminal phosphorylation lies within MuSK signaling pathway (Fig. 5, *E* and *F*).

TABLE 1
Top 10 kinase targets of AZ-23 in in vitro *kinase activity screen (n = 1)*

Kinase	0.1 μM	0.01 μM
	% Inhibition	
TrkC	102.8	97.9
TrkB	104.7	95.5
TrkA	101.6	65.7
MuSK	99.6	63.2
Ros	95.3	57.8
Flt3	89	49.2
PhKγ2	78.6	29.2
FGFR1	52	20.3
Lyn	68.4	16.7
ARK5	68.1	14.8

TABLE 2
Top 10 kinase targets of compound 28 in in vitro *kinase activity screen (n = 2)*

Kinase	0.1 μM	0.01 μM
	% Inhibition	
Flt3	99.3	97.4
Ret	95	75.1
MuSK	98.7	72.6
MAP4K4	95.4	64.6
Abl	94.3	58.8
Yes	98	58.3
ITK	97.7	52.3
Lck	94.7	47.8
Aurora_A	89.7	42
KDR	92.3	38.3

Rab10 Y6 is Essential for Interactions With Effectors Mical1 and Mical3

A Rab10 crystal structure has recently been reported in a complex with its effector Mical C-terminal-like protein (Mical-cL) (35). There it was observed that the N-terminal Rab subfamily motif 1 (RabSF1) region of Rab10 containing Y6 has extensive interactions with the C terminus of Mical-cL (Fig. 6*A*). The Mical-cL interacting surface contains multiple charged residues (Arg 671, Glu 668, and Glu 669), with the positively charged N termini of Rab10 and Rab8 forming a closer contact with the surface of Mical protein in comparison to negatively charged N terminus of Rab1 (35). Therefore, we hypothesized that Rab10 Y6 may modulate Rab protein interactions with their effector proteins.

To test this hypothesis, protein–protein interactions of HA-Rab10^{wt} and HA-Rab10^{Y6F} were compared in myotubes by IP–MS. We used MS1 area under the curve–based quantification to analyze Rab10 interactions as compared with Dox-negative background IP (*i.e.*, no HA-Rab10 expression). As expected, several known Rab10 effector molecules, including

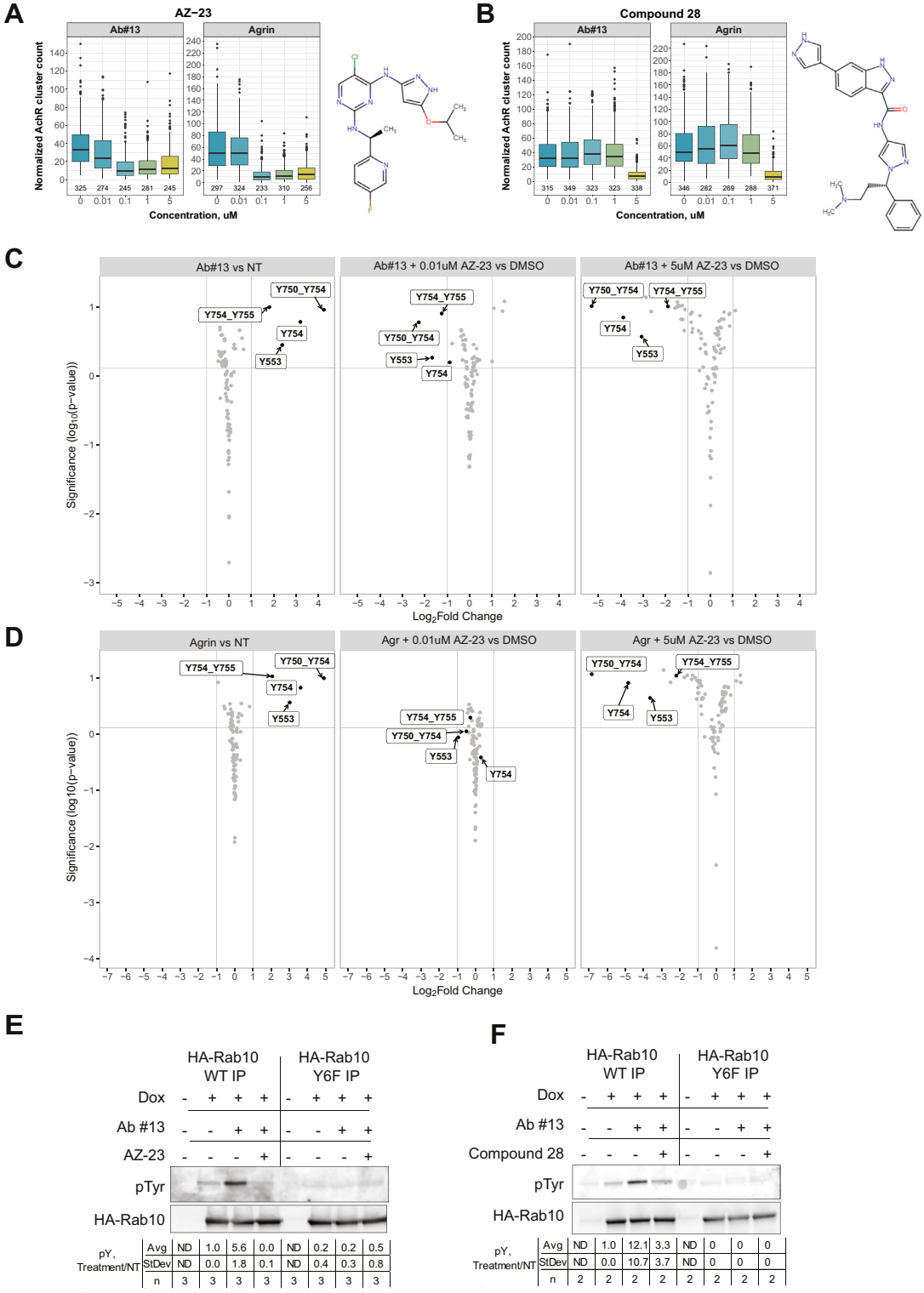

FIG. 5. **MuSK inhibition affects Rab10 tyrosine phosphorylation.** *A and B*, C2C12 myotubes were pretreated for 1 h with increasing concentrations of AZ-23 or compound 28 inhibitors, followed by treatment with 1 nM agrin or 5 nM Ab#13. Six hours after agonist treatment, AchR clusters were stained with anti-Bungarotoxin-Alexa Fluor 488. Total number of clusters per myotube was normalized to the number of nuclei stained with Hoescht. The median value per condition is indicated within the box plot, calculated based on three replicate experiments. The total number of quantified myotubes is indicated below the box plot. *C* and *D*, *left panel*, volcano plots of log2FC in site-specific phosphorylation of tyrosine kinases quantified by site in phosphoproteome profiling of C2C12 myotubes treated with 400 nM Ab#13 or 10 nM agrin, respectively, against untreated (NT) control. *Right panels*, log2FC in site-specific phosphorylation of tyrosine kinases by site in myotubes

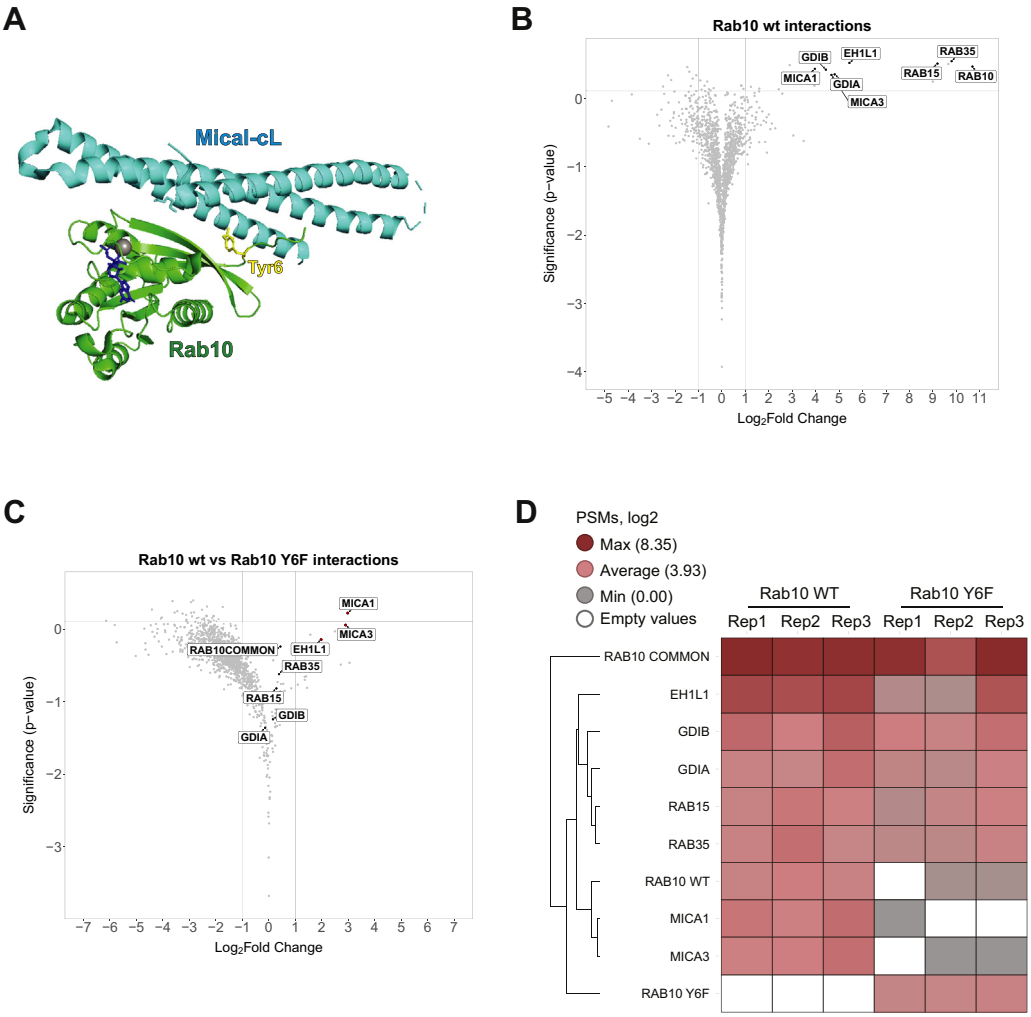

FIG. 6. **Y6 mediates Rab10 interactions with adaptor proteins.** *A*, crystal structure of Rab10 and Mical-cL complex with Rab10 Y6 highlighted in *yellow* (adapted from Ref. (35)). *B* and *C*, MS1 AUC-based interaction enrichment analysis of HA-Rab10^{wt} interactions compared with control (no HA-Rab10 expression) (*B*) or HA-Rab10^{Y6F} IP (*C*). Statistical analysis was performed using MSstats R package (n = 3). *D*, a heatmap of spectral counts per protein (PSMs, log2) quantified between Rab10^{wt} and Rab10^{Y6F} IPs in three replicate experiments. Rab10 COMMON denotes peptides that are common between Rab10^{wt} and Rab10^{Y6F}, whereas Rab10^{wt} and Rab10^{Y6F} indicate quantification of distinguishing peptides containing Y6 or the mutant Y6F, respectively. AUC, area under the curve; HA, hemagglutinin; IP, immunoaffinity purification; Mical-cL, Mical C-terminal-like protein; MS, mass spectrometry; PSM, peptide-to-spectrum match.

GDP-dissociation inhibitors (GDIs) 1 and 2, EH domain–binding protein–like protein 1, and Micals 1 and 3, were significantly enriched in Rab10^{WT} IP (log2 fold change ≥2, $p \leq 0.05$) (Fig. 6*B* and supplemental Table S3).

Importantly, when comparing the interaction landscape of Rab10^{wt} and Rab10^{Y6F} mutant, we observed a dramatic loss of interactions between the Rab10^{Y6F} mutant and Mical 1 and 3 but not with GDI molecules (Fig. 6, *C* and *D*). Between Rab10^{WT} and Rab10^{Y6F} IPs, average numbers of spectral counts for GDIA, GDIB, and EH domain–binding protein–like protein 1 were comparable (Fig. 6*D*). However, there was no more than a single peptide spectral match for Mical proteins in Rab10^{Y6F}, strongly contrasting with Rab10^{WT} IP samples (Fig. 6*D*). WB confirmed that this drop was not because of a change in total Mical protein levels (supplemental Fig. S5). Altogether, these observations support our hypothesis that

pretreated with indicated concentrations of AZ-23 or DMSO for 1 h, followed by treatment with each agonist for 30 min. Response of quantified MuSK phosphorylation sites is indicated in each plot. Statistical analysis of the data from two technical replicate experiments was performed using MSstatsTMT R package. *E* and *F*, C2C12 myotubes were treated with AZ-23, compound 28, or DMSO in the presence or the absence of MuSK Ab#13 for 1 h. Antiphosphotyrosine antibody was used to detect signal in each HA-Rab10 IP. Anti-HA antibody was used as a loading control for total HA-Rab10 levels. Statistics table indicates treated/NT (NT = +Dox, no treatment) pY ratios normalized to total HA-Rab10 levels, measured by ImageJ. Ab, antibody; AchR, acetylcholine receptor; DMSO, dimethyl sulfoxide; FC, fold change; HA, hemagglutinin; IP, immunoaffinity purification; MuSK, muscle-specific receptor tyrosine kinase.

the Y6 residue of Rab10 plays an important role in mediating interactions with Mical1 and Mical3 based on its location within the RabSF1 region.

DISCUSSION

In this study, we compared MuSK phosphorylation signaling initiated by either the endogenous agonist (agrin) or the MuSK agonist Ab#13. We observed that both agonists induce remarkably similar signaling cascades. This was an interesting finding since agrin and MuSK Abs were reported to act through different mechanisms of MuSK sequestration (11, 12). Agrin binds to LRP4, changing the conformation of LRP4–MuSK complex and inducing dimerization of the MuSK intracellular kinase domains. MuSK agonist Ab, on the other hand, binds directly to MuSK and does not require LRP4 for receptor activation (12). However, similarities of signaling profiles induced by each agonist are consistent with MuSK agonist Ab effectively delaying the onset of denervation in mouse models of ALS (12, 13), analogous to the effect of increasing MuSK expression (36). In light of these findings, therapeutic potential of MuSK agonist Ab could be further explored in congenital myasthenic syndrome instances associated with agrin and LRP4 variants that impair MuSK activation (37, 38).

In our orthogonal approach, we used a time course and a dose response with MuSK agonists to pinpoint MuSK-dependent signaling pathways in a time-resolved fashion. Moreover, we took this opportunity to characterize two small-molecule inhibitors as tool compounds for blocking MuSK activity in cells. We interrogated one of them (AZ-23) in detail, confirming its potency as a MuSK inhibitor in cell-based assays. AZ-23 was originally described as an inhibitor of Trks (34), a family with sequence similarity to MuSK based on their positions in the kinome tree (27). In addition, it was previously reported that expression of a chimeric receptor containing the MuSK juxtamembrane region and TrkA kinase domain in *MuSK*-mutant mice restored neuromuscular synapse formation (39). These observations provide additional evidence for the possible use of small-molecule inhibitors of Trks, such as AZ-23, in MuSK research. In addition to MuSK phosphorylation sites that are known to regulate its activity, we observed previously uncharacterized phosphorylation on Y599 in the ATP-binding region of the intracellular kinase domain. Phosphorylation of another tyrosine residue (Y576) on the opposite side of the ATP-binding motif was previously reported but observed to have little or no role in regulating AchR clustering (6). Rather, this tyrosine phosphorylation event might regulate other aspects of MuSK signaling, such as endocytosis and recycling of the activated receptor. In line with this hypothesis, our time-course analysis revealed that increased phosphorylation at these two sites occurs at later stages of MuSK activation (30–120 min post agonist treatment) as compared with early phosphorylation of tyrosine residues in the activation loop of the kinase domain.

Another observation pointing at the involvement of vesicular trafficking pathways in MuSK signaling is previously uncharacterized inducible tyrosine phosphorylation of Rab family of proteins. We identified that Rab8a, Rab10, Rab13, and Rab35 are phosphorylated in MuSK-dependent manner at the homologous N-terminal tyrosine sites. Micals and other adaptor proteins regulate transport of Rab-associated vesicles to particular intracellular membranes by linking them to the cytoskeleton (35). We demonstrated that the Y6 residue is necessary for mediating Rab10 interactions with Mical family Rab effector proteins. The stoichiometry of Y6 phosphorylation in RabSF1 region of Rab10 is estimated to be low based on Rab10 IP–MS results, where the phosphorylated species was detected in only one of the three replicate experiments. This experiment allows for only semiquantitative calculation of Rab10 Y6 phosphorylation abundance, which we estimate to be <1% of total Rab10 even after 30 min of MuSK activation (supplemental Fig. S6*A* and supplemental Table S4). In such a system, it is challenging to detect differential interactions of endogenous Mical proteins within a community of Rab effector proteins, most of whom are unphosphorylated even upon stimulation because they operate in different spatial communities than MuSK (supplemental Fig. S6*B* and supplemental Table S4) (40). We attempted to express Rab10 and Mical1 proteins from a single plasmid or by a double-plasmid transfection to improve reproducibility of Mical1 signal in Rab10 IP. However, we were not able to achieve high levels of expression in the first case and differentiate the myoblasts in the second case. Therefore, we were not able to confirm the dependence of Rab10–Mical interactions on Y6 phosphorylation status, and follow-up studies are required to test this hypothesis. Interestingly, it has been previously demonstrated that Rab phosphorylation by leucine-rich repeat kinase 2 on threonine in the switch II region does diminish Rab interactions with GDI proteins (41). We did not detect MuSK activation–dependent changes in phosphorylation levels at Rab10 T73 (supplemental Table S1), which suggests that this particular pathway is unlikely to play a role in MuSK signaling.

There are multiple processes involved in regulation of neuromuscular junction formation, maturation, and maintenance. In addition to AchR clustering, such processes include local transcriptional responses (42), accumulation of various synaptic proteins, cytoskeletal reorganization, and MuSK recycling (reviewed in Ref. (3)). Since some of these events can occur in parallel, it is possible that phosphorylation responses characterized in this study, such as phosphorylation of Rab proteins and AchR subunits, are not sequential. Further investigations are required to establish what aspects of Rab life cycle are directly impacted by MuSK-dependent phosphorylation and what type of cargo Rab-bound vesicles transport at the sites of MuSK activation. Interestingly, the consensus sequence of Rab tyrosine phosphorylation sites characterized in this study (YD) can be recognized by Src kinase (43), which was previously shown to play a role in MuSK signaling (26). On

the other hand, this motif is also present at Y406 in Dok7, which is a direct substrate of MuSK (44). Therefore, it is tempting to hypothesize that activated MuSK enters the Rab endocytic community in the process of internalization and recycling. Notably, phosphorylation of Rab10 on Y6 was also detected in a recent study of epidermal growth factor receptor–dependent signaling networks in rat tissues (45). Therefore, regulation of Rab function by tyrosine phosphorylation could be an important feature conserved in signaling networks mediated by different receptor tyrosine kinases.

DATA AVAILABILITY

Raw data files can be downloaded from the UCSD MassIVE mass spectrometry data repository (https://massive.ucsd.edu/ProteoSAFe/static/massive.jsp) using identifier MSV000085547. TIBCO Spotfire visualization dashboard is available for exploration of dose–response and time-course global proteome profiling and phosphoproteome profiling of MuSK signaling: https://sld-acs-sf.sf.perkinelmercloud.com/spotfire/wp/analysis?file=/Guest/MuSK_GlobalPhosphoProfiling&waid=7O5olDRpMUK6wRIS-ieLw-201250ef41XBf8&wavid=0.

Raw files were converted to mzXML using ReadW (version 4.3.1) available through https://sourceforge.net/projects/sashimi/files/ReAdW%20%28Xcalibur%20converter%29/.

Spectra were searched using Mascot (version 2.4.1) licensed from Matrix Sciences. Annotated spectra can be downloaded from the UCSD MassIVE using identifier MSV000085547.

Search results were filtered using the LDA function in the MASS Package in R (46).

Phosphorylation site localization probabilities were assigned by Ascore algorithm (18).

Mojave is an in-house tool developed to report TMT reporter ion intensity values and is available upon request.

MSstatsTMT (version 1.2.7) is a freely available open-source R/Bioconductor package to detect differentially abundant proteins in TMT experiments. It can be installed through https://www.bioconductor.org/packages/release/bioc/html/MSstatsTMT.html.

Supplemental data—This article contains supplemental data (19).

Acknowledgments—This work was funded by Genentech. We thank Erik Verschueren, Trent Hinkle, and Kebing Yu for computational support; Chris Rose, Tommy Cheung, and Taylur Ma for instrument optimization; Victoria Pham, Jiyeon Lee, Di Xue, and Andrey Shaw for scientific advice; Ben Haley for PiggyBac plasmid constructs; members of Antibody Discover and Protein Chemistry groups at Genentech for Ab#13 reagent; members of Microchemistry, Proteomics and Lipidomics department at Genentech for their continuous support and valuable feedback. PTMScan is performed at Genentech under limited license from Cell Signaling Technology. Graphical abstract was created with BioRender.com.

Author contributions—H. G. B., A. S.-G., G. A., and D. S. K. conceptualization; H. G. B., A. S.-G., G. A., and D. S. K. methodology; H. G. B., L. P., J. G. M. and D. S. K. formal analysis; H. G. B., A. S.-G., L. P., and J. G. M. investigation; H. G. B. and D. S. K. writing–original draft; H. G. B., A. S.-G., L. P., J. G. M., G. A., and D. S. K. writing–review and editing; D. S. K. supervision.

Conflict of interest—The authors declare no competing interests.

Abbreviations—The abbreviations used are: Ab, antibody; AchR, acetylcholine receptor; AGC, automatic gain control; Dok7, docking protein 7; FDR, false discovery rate; GDI, GDP-dissociation inhibitor; HA, hemagglutinin; IP, immunoaffinity purification; LRP4, low-density lipoprotein receptor–related protein 4; Mical, molecule interacting with CasL; Mical-cL, Mical C-terminal-like protein; MS, mass spectrometry; MuSK, muscle-specific receptor tyrosine kinase; NT, not treated; RabSF1, Rab subfamily motif 1; SPS-MS3, synchronous precursor selection MS/MS/MS; TMT, tandem mass tag; Trk, tropomyosin-related kinase; WB, Western blotting.

Received June 23, 2021, and in revised from, February 22, 2022
Published, MCPRO Papers in Press, February 26, 2022, https://doi.org/10.1016/j.mcpro.2022.100221

REFERENCES

1. Burden, S., Huijbers, M., and Remedio, L. (2018) Fundamental molecules and mechanisms for forming and maintaining neuromuscular synapses. *Int. J. Mol. Sci.* **19**, 490
2. Deenen, J. C. W., Horlings, C. G. C., Verschuuren, J. J. G. M., Verbeek, A. L. M., and van Engelen, B. G. M. (2015) The epidemiology of neuromuscular disorders: A comprehensive overview of the literature. *J. Neuromuscul. Dis.* **2**, 73–85
3. Herbst, R. (2019) Musk function during health and disease. *Neurosci. Lett.* **716**, 134676
4. Kim, N., Stiegler, A. L., Cameron, T. O., Hallock, P. T., Gomez, A. M., Huang, J. H., Hubbard, S. R., Dustin, M. L., and Burden, S. J. (2008) Lrp4 is a receptor for agrin and forms a complex with MuSK. *Cell* **135**, 334–342
5. Zhang, B., Luo, S., Wang, Q., Suzuki, T., Xiong, W. C., and Mei, L. (2008) LRP4 serves as a coreceptor of agrin. *Neuron* **60**, 285–297
6. Herbst, R. (2000) The juxtamembrane region of MuSK has a critical role in agrin-mediated signaling. *EMBO J.* **19**, 67–77
7. Okada, K., Inoue, A., Okada, M., Murata, Y., Kakuta, S., Jigami, T., Kubo, S., Shiraishi, H., Eguchi, K., Motomura, M., Akiyama, T., Iwakura, Y., Higuchi, O., and Yamanashi, Y. (2006) The muscle protein Dok-7 is essential for neuromuscular synaptogenesis. *Science* **312**, 1802–1805
8. Wallace, B. G. (1992) Mechanism of agrin-induced acetylcholine receptor aggregation. *J. Neurobiol.* **23**, 592–604
9. DeChiara, T. M., Bowen, D. C., Valenzuela, D. M., Simmons, M. V., Poueymirou, W. T., Thomas, S., Kinetz, E., Compton, D. L., Rojas, E., Park, J. S., Smith, C., DiStefano, P. S., Glass, D. J., Burden, S. J., and Yancopoulos, G. D. (1996) The receptor tyrosine kinase MuSK is required for neuromuscular junction formation *in vivo*. *Cell* **85**, 501–512
10. Glass, D. J., Bowen, D. C., Stitt, T. N., Radziejewski, C., Bruno, J., Ryan, T. E., Gies, D. R., Shah, S., Mattsson, K., Burden, S. J., DiStefano, P. S., Valenzuela, D. M., DeChiara, T. M., and Yancopoulos, G. D. (1996) Agrin acts *via* a MuSK receptor complex. *Cell* **85**, 513–523

11. Xie, M.-H., Yuan, J., Adams, C., and Gurney, A. (1997) Direct demonstration of MuSK involvement in acetylcholine receptor clustering through identification of agonist ScFv. *Nat. Biotechnol.* **15**, 768–771
12. Cantor, S., Zhang, W., Delestrée, N., Remédio, L., Mentis, G. Z., and Burden, S. J. (2018) Preserving neuromuscular synapses in ALS by stimulating MuSK with a therapeutic agonist antibody. *eLife Sci.* **7**, e34375
13. Sengupta-Ghosh, A., Dominguez, S. L., Xie, L., Barck, K. H., Jiang, Z., Earr, T., Imperio, J., Phu, L., Budayeva, H. G., Kirkpatrick, D. S., Cai, H., Eastham-Anderson, J., Ngu, H., Foreman, O., Hedehus, M., *et al*. (2019) Muscle specific kinase (MuSK) activation preserves neuromuscular junctions in the diaphragm but is not sufficient to provide a functional benefit in the SOD1G93A mouse model of ALS. *Neurobiol. Dis.* **124**, 340–352
14. Pastor, R. M., Burch, J. D., Magnuson, S., Ortwine, D. F., Chen, Y., De La Torre, K., Ding, X., Eigenbrot, C., Johnson, A., Liimatta, M., Liu, Y., Shia, S., Wang, X., Wu, L. C., and Pei, Z. (2014) Discovery and optimization of indazoles as potent and selective interleukin-2 inducible T cell kinase (ITK) inhibitors. *Bioorg. Med. Chem. Lett.* **24**, 2448–2452
15. Paulo, J. A., and Gygi, S. P. (2017) Nicotine-induced protein expression profiling reveals mutually altered proteins across four human cell lines. *Proteomics* **17**, 1600319
16. McAlister, G. C., Nusinow, D. P., Jedrychowski, M. P., Wühr, M., Huttlin, E. L., Erickson, B. K., Rad, R., Haas, W., and Gygi, S. P. (2014) MultiNotch MS3 enables accurate, sensitive, and multiplexed detection of differential expression across cancer cell line proteomes. *Anal. Chem.* **86**, 7150–7158
17. Kirkpatrick, D. S., Bustos, D. J., Dogan, T., Chan, J., Phu, L., Young, A., Friedman, L. S., Belvin, M., Song, Q., Bakalarski, C. E., and Hoeflich, K. P. (2013) Phosphoproteomic characterization of DNA damage response in melanoma cells following MEK/PI3K dual inhibition. *Proc. Natl. Acad. Sci. U. S. A.* **110**, 19426–19431
18. Beausoleil, S. A., Villén, J., Gerber, S. A., Rush, J., and Gygi, S. P. (2006) A probability-based approach for high-throughput protein phosphorylation analysis and site localization. *Nat. Biotechnol.* **24**, 1285–1292
19. Dürnberger, G., Camurdanoglu, B. Z., Tomschik, M., Schutzbier, M., Roitinger, E., Hudecz, O., Mechtler, K., and Herbst, R. (2014) Global analysis of muscle-specific kinase signaling by quantitative phosphoproteomics. *Mol. Cell Proteomics* **13**, 1993–2003
20. Abràmoff, D. M. D. (2004) Image processing with ImageJ. *Biophotonics Int.* **11**, 36–42
21. Abed, M., Verschueren, E., Budayeva, H., Liu, P., Kirkpatrick, D. S., Reja, R., Kummerfeld, S. K., Webster, J. D., Gierke, S., Reichelt, M., Anderson, K. R., Newman, R. J., Roose-Girma, M., Modrusan, Z., Pektas, H., *et al*. (2019) The Gag protein PEG10 binds to RNA and regulates trophoblast stem cell lineage specification. *PLoS One* **14**, e0214110
22. Bakalarski, C. E., Elias, J. E., Villén, J., Haas, W., Gerber, S. A., Everley, P. A., and Gygi, S. P. (2008) The impact of peptide abundance and Dynamic range on stable-isotope-based quantitative proteomic analyses. *J. Proteome Res.* **7**, 4756–4765
23. Choi, M., Chang, C.-Y., Clough, T., Broudy, D., Killeen, T., MacLean, B., and Vitek, O. (2014) MSstats: an R package for statistical analysis of quantitative mass spectrometry-based proteomic experiments. *Bioinformatics* **30**, 2524–2526
24. Sievers, F., Wilm, A., Dineen, D., Gibson, T. J., Karplus, K., Li, W., Lopez, R., McWilliam, H., Remmert, M., Söding, J., Thompson, J. D., and Higgins, D. G. (2011) Fast, scalable generation of high-quality protein multiple sequence alignments using Clustal Omega. *Mol. Syst. Biol.* **7**, 539
25. Ting, L., Rad, R., Gygi, S. P., and Haas, W. (2011) MS3 eliminates ratio distortion in isobaric labeling-based multiplexed quantitative proteomics. *Nat. Methods* **8**, 937–940
26. Mohamed, A. S., Rivas-Plata, K. A., Kraas, J. R., Saleh, S. M., and Swope, S. L. (2001) Src-class kinases act within the agrin/MuSK pathway to regulate acetylcholine receptor phosphorylation, cytoskeletal anchoring, and clustering. *J. Neurosci.* **21**, 3806–3818
27. Manning, G., Whyte, D. B., Martinez, R., Hunter, T., and Sudarsanam, S. (2002) The protein kinase complement of the human genome. *Science* **298**, 1912–1934
28. Hallock, P. T., Chin, S., Blais, S., Neubert, T. A., and Glass, D. J. (2016) Sorbs1 and -2 interact with CrkL and are required for acetylcholine receptor cluster formation. *Mol. Cell Biol.* **36**, 262–270
29. Kishi, M., Kummer, T. T., Eglen, S. J., and Sanes, J. R. (2005) LL5 beta: a regulator of postsynaptic differentiation identified in a screen for synaptically enriched transcripts at the neuromuscular junction. *J. Cell Biol.* **169**, 355–366
30. Adams, M. E., Kramarcy, N., Krall, S. P., Rossi, S. G., Rotundo, R. L., Sealock, R., and Froehner, S. C. (2000) Absence of alpha-syntrophin leads to structurally aberrant neuromuscular synapses deficient in utrophin. *J. Cell Biol.* **150**, 1385–1398
31. Hirata, Y., Brotto, M., Weisleder, N., Chu, Y., Lin, P., Zhao, X., Thornton, A., Komazaki, S., Takeshima, H., Ma, J., and Pan, Z. (2006) Uncoupling store-operated Ca2+ entry and altered Ca2+ release from sarcoplasmic reticulum through silencing of junctophilin genes. *Biophys. J.* **90**, 4418–4427
32. Prasad, N. K. (2009) SHIP2 phosphoinositol phosphatase positively regulates EGFR-Akt pathway, CXCR4 expression, and cell migration in MDA-MB-231 breast cancer cells. *Int. J. Oncol.* **34**, 97–105
33. Monier, S., Jollivet, F., Janoueix-Lerosey, I., Johannes, L., and Goud, B. (2002) Characterization of novel Rab6-interacting proteins involved in endosome-to-TGN transport. *Traffic* **3**, 289–297
34. Thress, K., MacIntyre, T., Wang, H., Whitston, D., Liu, Z.-Y., Hoffmann, E., Wang, T., Brown, J. L., Webster, K., Omer, C., Zage, P. E., Zeng, L., and Zweidler-McKay, P. A. (2009) Identification and preclinical characterization of AZ-23, a novel, selective, and orally bioavailable inhibitor of the Trk kinase pathway. *Mol. Cancer Ther.* **8**, 1818–1827
35. Rai, A., Oprisko, A., Campos, J., Fu, Y., Friese, T., Itzen, A., Goody, R. S., Gazdag, E. M., and Müller, M. P. (2016) bMERB domains are bivalent Rab8 family effectors evolved by gene duplicationJahn, R., ed.. *eLife* **5**, e18675
36. Perez-Garcia, M. J., and Burden, S. J. (2012) Increasing MuSK activity delays denervation and improves motor function in ALS mice. *Cell Rep.* **2**, 497–502
37. Ohkawara, B., Cabrera-Serrano, M., Nakata, T., Milone, M., Asai, N., Ito, K., Ito, M., Masuda, A., Ito, Y., Engel, A. G., and Ohno, K. (2014) LRP4 third β-propeller domain mutations cause novel congenital myasthenia by compromising agrin-mediated MuSK signaling in a position-specific manner. *Hum. Mol. Genet.* **23**, 1856–1868
38. Ohkawara, B., Shen, X., Selcen, D., Nazim, M., Bril, V., Tarnopolsky, M. A., Brady, L., Fukami, S., Amato, A. A., Yis, U., Ohno, K., and Engel, A. G. (2020) Congenital myasthenic syndrome–associated agrin variants affect clustering of acetylcholine receptors in a domain-specific manner. *JCI Insight [Internet]* **5**, e132023
39. Herbst, R., Avetisova, E., and Burden, S. J. (2002) Restoration of synapse formation in Musk mutant mice expressing a Musk/Trk chimeric receptor. *Development* **129**, 5449–5460
40. Budayeva, H. G., and Kirkpatrick, D. S. (2020) Monitoring protein communities and their responses to therapeutics. *Nat. Rev. Drug Discov.* **19**, 414–426
41. Steger, M., Tonelli, F., Ito, G., Davies, P., Trost, M., Vetter, M., Wachter, S., Lorentzen, E., Duddy, G., Wilson, S., Baptista, M. A., Fiske, B. K., Fell, M. J., Morrow, J. A., Reith, A. D., *et al*. (2016) Phosphoproteomics reveals that Parkinson's disease kinase LRRK2 regulates a subset of Rab GTPasesDikic, I., ed.. *eLife* **5**, e12813
42. Hippenmeyer, S., Huber, R. M., Ladle, D. R., Murphy, K., and Arber, S. (2007) ETS transcription factor erm controls subsynaptic gene expression in skeletal muscles. *Neuron* **55**, 726–740
43. Schwartz, D., and Gygi, S. P. (2005) An iterative statistical approach to the identification of protein phosphorylation motifs from large-scale data sets. *Nat. Biotechnol.* **23**, 1391–1398
44. Hamuro, J., Higuchi, O., Okada, K., Ueno, M., Iemura, S., Natsume, T., Spearman, H., Beeson, D., and Yamanashi, Y. (2008) Mutations causing DOK7 congenital myasthenia ablate functional motifs in Dok-7. *J. Biol. Chem.* **283**, 5518–5524
45. Lundby, A., Franciosa, G., Emdal, K. B., Refsgaard, J. C., Gnosa, S. P., Bekker-Jensen, D. B., Secher, A., Maurya, S. R., Paul, I., Mendez, B. L., Kelstrup, C. D., Francavilla, C., Kveiborg, M., Montoya, G., Jensen, L. J., *et al*. (2019) Oncogenic mutations rewire signaling pathways by switching protein recruitment to phosphotyrosine sites. *Cell* **179**, 543–560.e26
46. Huttlin, E. L., Jedrychowski, M. P., Elias, J. E., Goswami, T., Rad, R., Beausoleil, S. A., Villén, J., Haas, W., Sowa, M. E., and Gygi, S. P. (2010) A Tissue-specific atlas of mouse protein phosphorylation and expression. *Cell* **143**, 1174–1189